Ultramicroscopy 163 (2016) 6–18

Contents lists available at ScienceDirect

Ultramicroscopy

journal homepage: www.elsevier.com/locate/ultramic

3D imaging by serial block face scanning electron microscopy for materials science using ultramicrotomy

Teruo Hashimoto*, George E. Thompson, Xiaorong Zhou, Philip J. Withers

School of Materials, The University of Manchester, Manchester M13 9PL, England, UK

ARTICLE INFO

Article history:
Received 24 June 2015
Received in revised form
25 January 2016
Accepted 28 January 2016
Available online 29 January 2016

Keywords:
SBFSEM
Ultramicrotomy
Material science

ABSTRACT

Mechanical serial block face scanning electron microscopy (SBFSEM) has emerged as a means of obtaining three dimensional (3D) electron images over volumes much larger than possible by focused ion beam (FIB) serial sectioning and at higher spatial resolution than achievable with conventional X-ray computed tomography (CT). Such high resolution 3D electron images can be employed for precisely determining the shape, volume fraction, distribution and connectivity of important microstructural features. While soft (fixed or frozen) biological samples are particularly well suited for nanoscale sectioning using an ultramicrotome, the technique can also produce excellent 3D images at electron microscope resolution in a time and resource-efficient manner for engineering materials. Currently, a lack of appreciation of the capabilities of ultramicrotomy and the operational challenges associated with minimising artefacts for different materials is limiting its wider application to engineering materials. Consequently, this paper outlines the current state of the art for SBFSEM examining in detail how damage is introduced during slicing and highlighting strategies for minimising such damage. A particular focus of the study is the acquisition of 3D images for a variety of metallic and coated systems.

1. Introduction

Ultramicrotomy is now widely utilised in life sciences to prepare specimens for transmission electron microscopy (TEM). This is in part due to the physical characteristics of either fixed or frozen biological materials which, being relatively soft, enable the routine preparation of electron transparent specimens [1]. For similar reasons, ultramicrotomy is also commonly employed for the preparation of polymer TEM specimens [2–5]. On the other hand, engineering materials, for example light alloys and hard coatings, present a sterner challenge. Nevertheless, ultramicrotomy has been successfully used to prepare electron transparent specimens for examining the morphologies of the coatings attached to metal substrates [6,7]. The benefits associated with the preparation of thin, electron transparent ultramicrotomed slices using a sharp diamond knife include the short specimen preparation time and the capacity to observe relatively large areas, typically of 300×50 μm dimensions, compared with other preparation techniques such as focused ion beam (FIB) microscopy. However, the mechanical slicing can introduce damage and, hence, artefacts on the thin slices and the remaining block face from which the slices are generated. Typical artefacts in thin ultramicrotomed slices include chattering, compression of the chip material, knife marks and lifting up of hard particles from the adjacent relatively soft matrix [8–11]. Using ultramicrotomy for the generation of thin slices of hard materials, the plastic deformation generated by compression/shear under the knife can seriously distort the size and shape of objects, and locally deforms the crystal structure.

Considering the use of automated ultramicrotomy (inSEM) for 3D block face serial section imaging by scanning electron microscopy (SBFSEM), the block face typically displays fewer artefacts than the thin slices. However, issues still remain, including the introduction of knife marks and damage. In cases where strategies can be developed to minimise such artefacts serial sectioning can provide a great deal of 3D information of interest to the materials scientist from volumes much larger than can be accessed by FIB serial sectioning and at higher resolution than can be achieved routinely by laboratory X-ray computed tomography [12]. A major advance in the routine application of the SBFSEM method has been made in the biological field by automating the block-face sectioning and the imaging process within the scanning electron microscope [13]. This offers very significant alignment benefits and time-saving over manual sectioning [14]. Commercial automated systems are now available, such as the Gatan 3View system [13,15] and the FEI VolumeScope system [16], where automated sectioning and capture systems are located in a variable pressure, field emission gun, environmental scanning electron microscope (FEG-ESEM). Sequential ultramicrotomy and imaging produce a

* Corresponding author.
E-mail address: t.hashimoto@manchester.ac.uk (T. Hashimoto).

http://dx.doi.org/10.1016/j.ultramic.2016.01.005

stack of aligned images that can be viewed in sequence, or further processed using 3D reconstruction and analysis software. Automation has allowed acquisition workflows delivering very large 3D datasets at electron microscope resolution, for example to reconstruct the connectivity of neuronal circuits in brain mapping [13]. Such datasets are now being collected by SEM or TEM comprising up to 10,000 sections covering 400 μm dimensions at 4 nm resolution and 100 TB in size [17].

While the approach has been exploited widely in the biological and medical science fields, providing detailed images of tissues [18] and whole organisms [19] as well as in polymer science [20–24], the technique has been much less widely used in materials science and metallurgy due to the difficulty of ultramicrotoming the harder materials as described above. However, Thompson and co-workers have been at the vanguard of developing workflows to investigate the corrosion behaviour of aluminium [14,25–27] and magnesium [28], the influence of organic coatings on corrosion pathways [29], the distribution of pigments in the paint [30–32], and the distribution of intermetallics during casting or forming [33–35].

There is currently a gap between non-destructive X-ray tomography and destructive serial sectioning by FIB [36]. Laboratory and synchrotron X-ray imaging can routinely provide morphological data at scales down to sub-micron levels for samples of millimetre dimensions [37]. Advanced X-ray tomography techniques can also provide grain shapes and orientations [38] and chemistry [39] over tens of micron scales. On the other hand, FIB SBFSEM can provide chemical, crystallographic and morphological information at the 5 nm length scale, but only over volumes of tens of microns. Importantly, emerging plasma FIB [40] or laser [41] dual beam microscopies may extend this to dimensions of hundreds of microns. However, the method has high capital and running costs, and is time consuming. Thus, the extension of SBFSEM with ultramicrotomy to a wide range of materials science fields offers the potential of 3D imaging at electron microscopy resolution in a time and resource efficient manner. Currently, the lack of appreciation of the capabilities of the technique and the operational challenges associated with minimising artefacts for different materials are limiting the wider uptake of serial block face scanning electron microscopy of engineering materials. This paper aims to capture the current state of the art for SBFSEM via ultramicrotomy in materials science and to examine in detail the ways in which damage is introduced during slicing, and to outline strategies for minimising damage with a particular focus on the high strength to weight ratio, commercially important AA2024 aluminium alloy as an example. This is followed by an examination of the extent to which SBFSEM can be applied to a wide range of materials science applications.

2. The experimental setup

Fig. 1 shows a schematic diagram of the ultramicrotomy-based serial block face scanning electron microscope. It is noted that the size of the block face, the slice thickness and observation conditions are dependent on the region of interest, the properties of the material and the size of the object.

For the ultramicrotoming study, the block face of an AA2024 aluminium alloy test-piece was prepared to dimensions of approximately 100×400 um using mechanical grinding to generate the pyramid shape, and then conventional ultramicrotomy with a glass knife was used to trim the specimen to approximately 50×200 um. Finally, in order to remove the residual damage generated by the above process, the block face was sliced with a diamond knife at a cutting speed of 0.2 mm/s for 50 slices of 15 nm thickness. The typical observation conditions were at an acceleration voltage of 2.5 keV with a constant slice thickness of 15 nm.

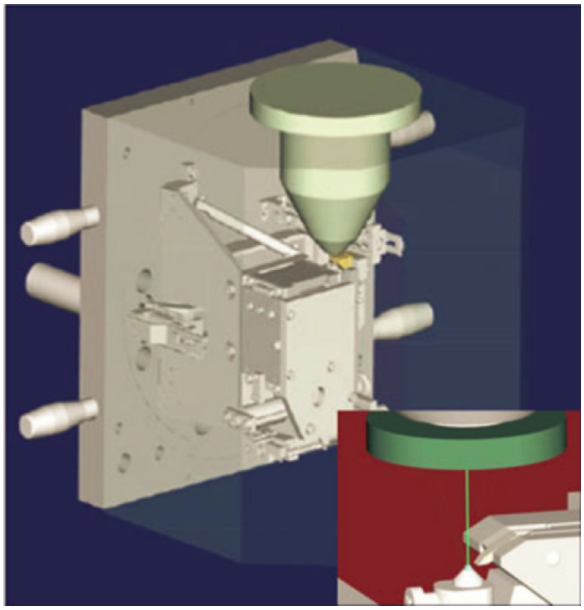

Fig. 1. Schematic diagram of the inSEM ultramicrotome (Gatan 3View) located on the chamber door of an (FEI Quanta 250) FEG-ESEM. The inset shows the positioning of the specimen in the electron beam and the location of the motor driven diamond knife, which is able to generate serial sections without the need for realignment of the specimen under the electron beam [16].

3. Resolution of SBFSEM imaging

The spatial resolution of SBFSEM imaging is determined by the lateral (X and Y) spatial resolutions and the probe depth and slice thickness in the Z direction [42]. The spatial resolution of a back scattered electron (BSE) image is well known to be related to the probe size of the electron beam and the three dimensional volume of the back scattered electron output because scattering within the specimen is larger than the diameter of the illuminating probe. The BSE volume decreases with increasing atomic number and increases with accelerating voltage. For example, at 1 keV the maximum penetration depths of BSEs generated in amorphous carbon, aluminium and copper substrates are approximately 9, 7 and 2.4 nm respectively. With regard to the depth (Z) resolution, the beam penetration depth rather than the slice thickness is usually the determining factor. When the object size is smaller than the beam penetration depth, the BSE signals result from both the object of interest and the surrounding matrix, influencing the BSE coefficient. Consequently, a large penetration depth will limit the ability to resolve two objects regardless of the slice thickness. In order to examine the influence of beam penetration on spatial resolution, the 5 nm serial sectioning of an Al (10 nm)/$CuAl_2$ (10 nm) alternating multilayer sample is considered in Fig. 2, with the grey scale exhibited as a function of accelerating voltage. At 1 keV, the signal arises largely from the top layer at a time regardless of the slice location. However, with increasing accelerating voltage the contrast recorded between the layers decreases due to electrons being scattered from both layers irrespective of the slice location. The accelerating voltage at which the two layers cannot be resolved depends on the greyscale threshold level used to segment the layers, but it is clear that even at 2 kV the contrast between the layers is significantly reduced. Determination of the threshold level is critical with respect to the Z resolution. However, for an unknown composition of an intermetallic in the alloy system it is impossible to know the beam penetration value. Equally, having a large slice thickness and a low beam penetration would also mean that small objects could be missed. Thus, matching the slice thickness to the

beam penetration in the matrix material is a sensible approach.

While the most direct way of improving the Z resolution is to reduce the penetration depth by reducing the accelerating voltage one can also change the energy of the backscattered electrons detected. This increases the Z resolution because the higher energy level BSEs emanate from regions very near to the specimen surface. However, both techniques result in low signal-to-noise ratio (SNR). The SNR may be improved by increasing the beam current. In order to increase the beam current, an aberration corrected electron beam is ideal. Importantly, the influence of contamination with hydrocarbons introduced by the electron beam onto the specimen surface can be significant when a low acceleration voltage and increased beam current are employed. However, this is not a major concern for serial sectioning because a fresh block face is repeatedly generated in the SEM chamber. Therefore, the maximum current of the electron beam can be used. Clearly, the use of an aberration corrected electron beam with a combination of low voltage and energy selected BSE detection is ideal for realising the full potential of SBFSEM.

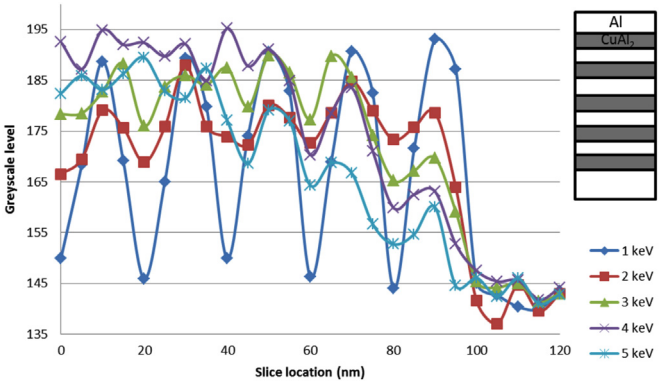

Fig. 2. Influence of primary electron beam penetration on the BSE signal (greyscale level) recorded for serial sectioning using a 5 nm slice thicknessat different acceleration voltages for a 10 nm repeating Al (white)/$CuAl_2$ (grey) multi- layer model system (see inset).

4. Artefacts from slicing

Observation of the block face using the BSE signal is sensitive to the microscale surface roughness since this changes the electron scattering angle. The surface roughness caused by ultramicrotoming the AA2024 aluminium test-piece has been assessed by atomic force microscopy (AFM) and Kelvin probe microscopy (KPM) in Fig. 3. The surface roughness recorded by AFM is around 1.2 nm over the green region in Fig. 3(a), which does not contain any gross knife marks. The Volta potential in the corresponding KPM map confirms that the roughness is mainly associated with the intermetallics. It is noteworthy that other commonly used surface preparation techniques, such as electropolishing or mechanical polishing, typically result in much greater average roughness values (about 100 nm and 230–280 nm respectively). The knife marks are caused by smearing of the block face by the lift out of hard intermetallics that adhere to the knife edge. In this case the hard, mainly copper- and magnesium-containing intermetallics are randomly distributed in the matrix and, therefore, the associated knife marks cannot be avoided. However, as shown in Fig. 4, image processing can effectively remove these linear features.

Other artefacts typical of slicing by ultramicrotomy, namely chattering and compression of chip materials, are often observed. Chattering is evident from the unevenness of the slice, which is caused by the mechanical instability of the knife and the specimen during slicing. Slow speed cutting can reduce chatter. The compression of the chip material arises from the strong force applied between the cut surface and the chip. The compression rate (cutting speed) influences the chattering of the block face. The associated surface texture is clearly evident in each grain in Fig. 4. Suppressing such chatter is the biggest challenge when slicing metallic samples and this is discussed below.

5. Principles of cutting

Merchant [43,44] developed an orthogonal cutting model that assumes that the knife is sharp and no rubbing occurs between the knife and the specimen. A sharp knife is defined as one where the slice thickness is more than 10 times the radius of the knife-edge. The radius of the diamond knife with an edge of 45 degrees is

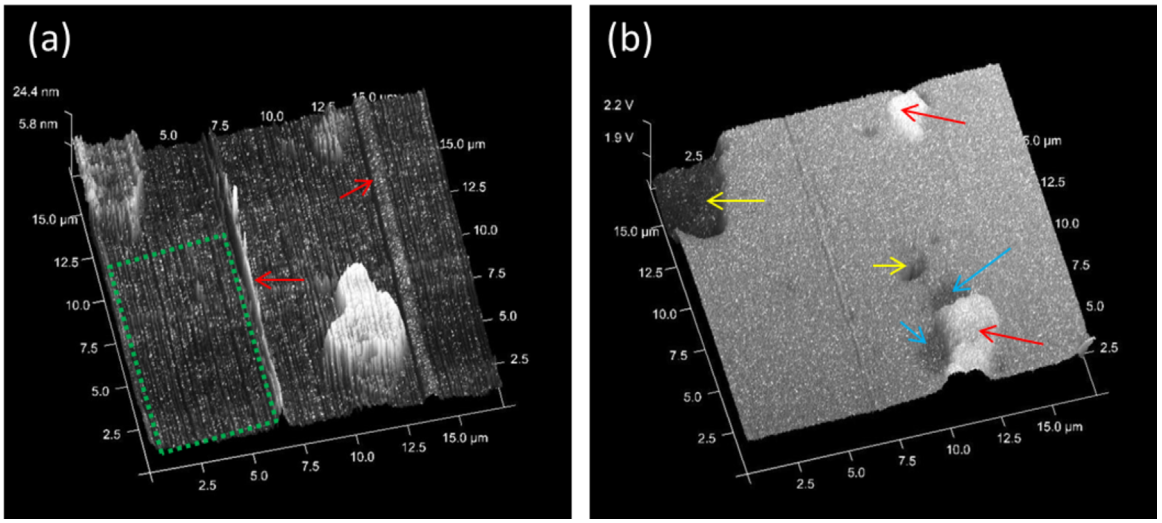

Fig. 3. (a) AFM topographic and (b) scanning Kelvin probe potential images from the 17.5 × 17.5 mm block face of the AA2024 aluminium alloy after utramicrotoming 10 slices of 20 nm thickness. Much of the roughness relates to the diamond knife marks indicated by red arrows in (a) and lift out of S, θ and α phases which are indicated by the red, blue and yellow arrows respectively in (b). The intermetallic phases were determined from the potential difference in (b). The overall mean roughness, Ra, is 3.2 nm while the aluminium matrix (green region) has a mean roughness of 1.2 nm. (For interpretation of the references to colour in this figure legend, the reader is referred to the web version of this article.)

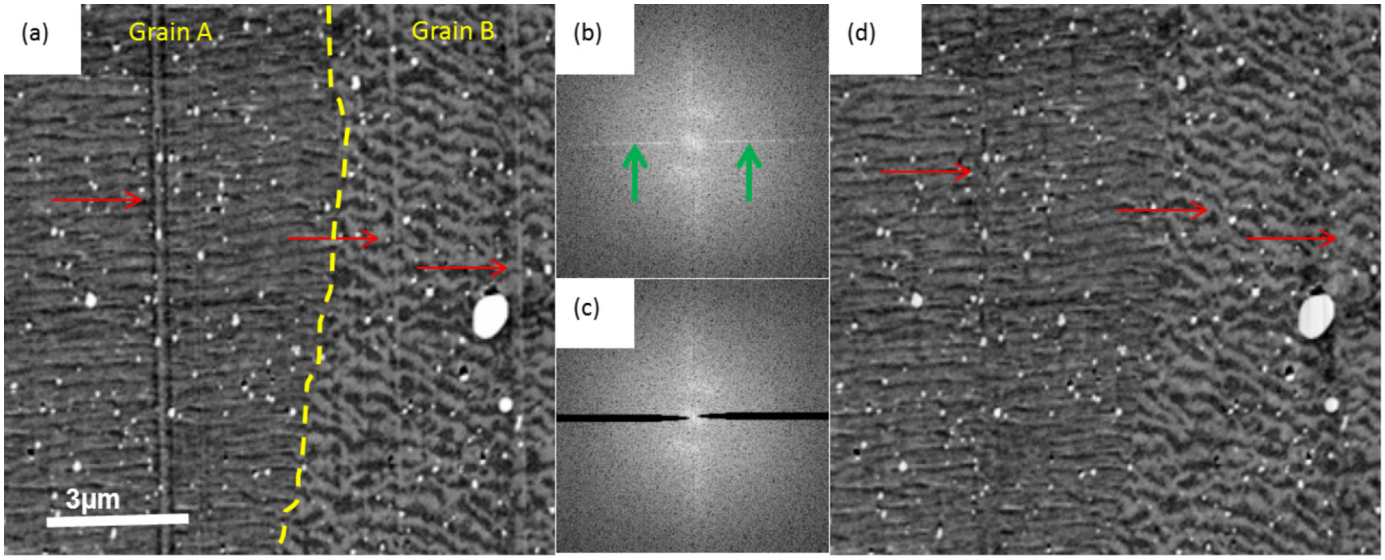

Fig. 4. BSE scanning electron micrographs of the block face of the AA2024 aluminium alloy test-piece: (a) as- acquired image showing knife features (red arrows); (b) FFT of image with the knife features indicated by the green arrows; (c) masking of the knife related features; and (d) inverse FFT of (c). The yellow dashed line denotes a grain boundary. (For interpretation of the references to colour in this figure legend, the reader is referred to the web version of this article.)

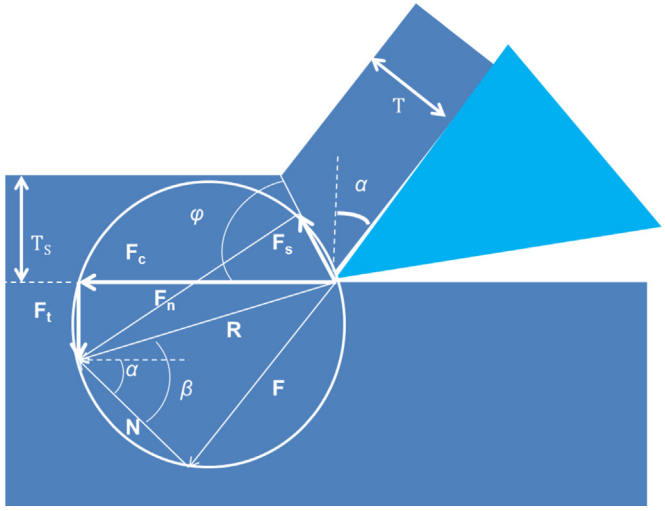

Fig. 5. Schematic force diagram showing Merchant's orthogonal cutting.

measured to be approximately 3 nm [45]. Using the Merchant cutting model, the force, and angle and velocity relationships can be estimated for slice thicknesses greater than 30 nm, as displayed in Figs. 5 and 6 respectively.

The resultant force, R, can be resolved into two force components, namely the cutting force along the cutting direction, F_c, and that perpendicular to the cutting direction, F_t. These forces are expressed as follows:

$$F_c=\frac{\tau_m T b \cos(\beta-\alpha)}{\sin(\varphi)\cos(\varphi+\beta-\alpha)} \quad (1)$$

$$F_t=\frac{\tau_m T b \sin(\beta-\alpha)}{\sin(\varphi)\cos(\varphi+\beta-\alpha)} \quad (2)$$

where φ is the shear angle, α is the tool rake angle (41°, with a 4° clearance angle (the angle between the back face of the knife and the block face)) giving a 45° knife angle, β is the angle between the resultant force and the normal to the rake face, τ_m is the shear strength of the material, T is the thickness of the slice removed and b is the width of the cut tool (diamond knife). The resultant force, R, can also be resolved into a friction force, F, and a normal force, N, perpendicular to it or equivalently with respect to the shear plane into a shear force, F_s, and a force normal to the shear force, F_n.

The shear angle, φ, is an important variable in metal cutting analysis because it defines the deformation characteristics of the chips. The relationship between the angles is then given by the following equation:

$$\varphi=\frac{\pi}{4}-\frac{1}{2}(\beta-\alpha) \quad (3)$$

The compression rate, c, can be determined from the length of cut or chip thickness, as follows:

$$c=\frac{l}{l_{chip}}=\frac{T_s}{T}=\frac{\sin\alpha}{\cos(\alpha-\varphi)} \quad (4)$$

where l is the length of the cut, l_{chip} is the length of the chip, T is the depth of the removed slice, T_s is the chip thickness and c is the compression rate. It is difficult to evaluate the compression rate from the slice length or thickness because it is not possible to collect the individual chips (representing the removed slices) from within the SEM. Therefore, the compression rate was determined from the shear angle and chip thickness measurements obtained by stopping the cutting process for different slicing thicknesses and examining the attached chips in the SEM (Fig. 7). Once the shear angle has been determined, all the forces may then be estimated enabling understanding of how damage is introduced into the block face. It is noteworthy that for slice thicknesses ranging from 50 nm to 10 μm no significant change in the shear angle was measured (Fig. 7). This confirms that the cutting forces have a linear relationship with the thickness for slices thicker than 50 nm.

As mentioned previously, this analysis applies to slices greater than 10 times the knife radius. This is because the curved knife edge changes the effective knife angle during the cutting process. In order to estimate the forces for ultra-thin slices (<30 nm), the rake angle was estimated from the following relationship:

$$\cot\alpha=\frac{T-r}{\sqrt{2rT-T^2}} \quad (5)$$

where r is the radius of the diamond knife edge. From this relationship, with 3 nm thickness slicing, the rake angle becomes 0°.

The reduction of the thickness increases the effective rake angle and, consequently, reduces the shear angle. Thus, selecting very thin slices increases the thrust and friction forces, which lead to an increase in damage to the block face. Slice thicknesses of 2.5 nm have been reported [27], whereas sectioning below 2.5 nm has not yet been successful. This might indicate the need for a minimum shear angle or maximum knife angle to enable the material to be sliced. In such cases, the thrust and friction forces may become greater than the cutting force and, consequently, the knife edge would rub along the block face instead of cutting it. Further, the slicing involves plastic deformation ahead of the diamond knife tip and elastic recovery of the block face after the knife has passed, resulting in a slight upward movement of material at the block face near the diamond knife tip. Importantly, the shear plane appears to start at a point above the diamond knife tip due to an increase of the thrust force as a consequence of reduction of the rake angle. Fig. 8 shows a schematic diagram of the force relations whilst taking account of the influence of the radius of the diamond knife. We assume that the difference between the thicknesses of the shear force starting point and the recovering layer is an atomic

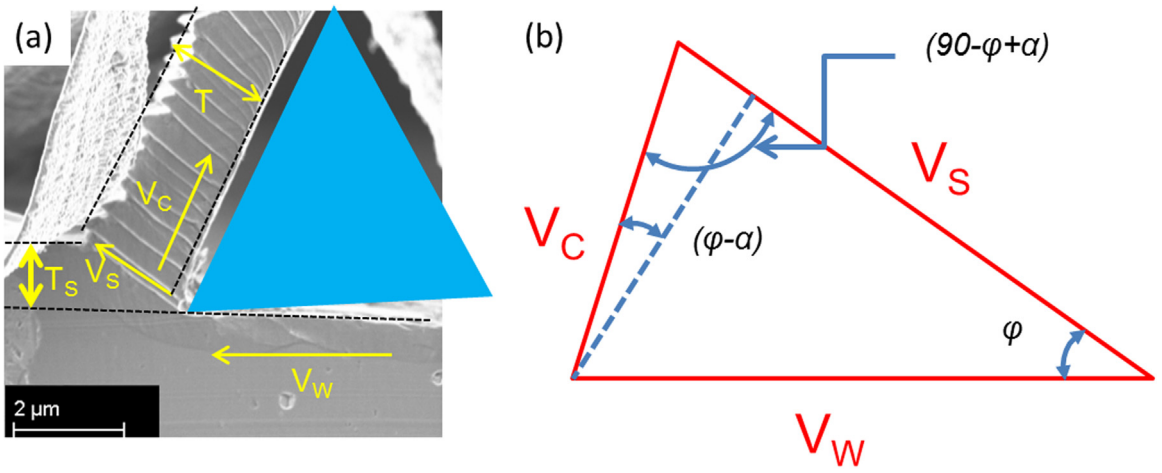

Fig. 6. Schematic diagrams showing the relationship between the angles and the velocity in shear zone: (a) velocity and (b) angle diagrams.

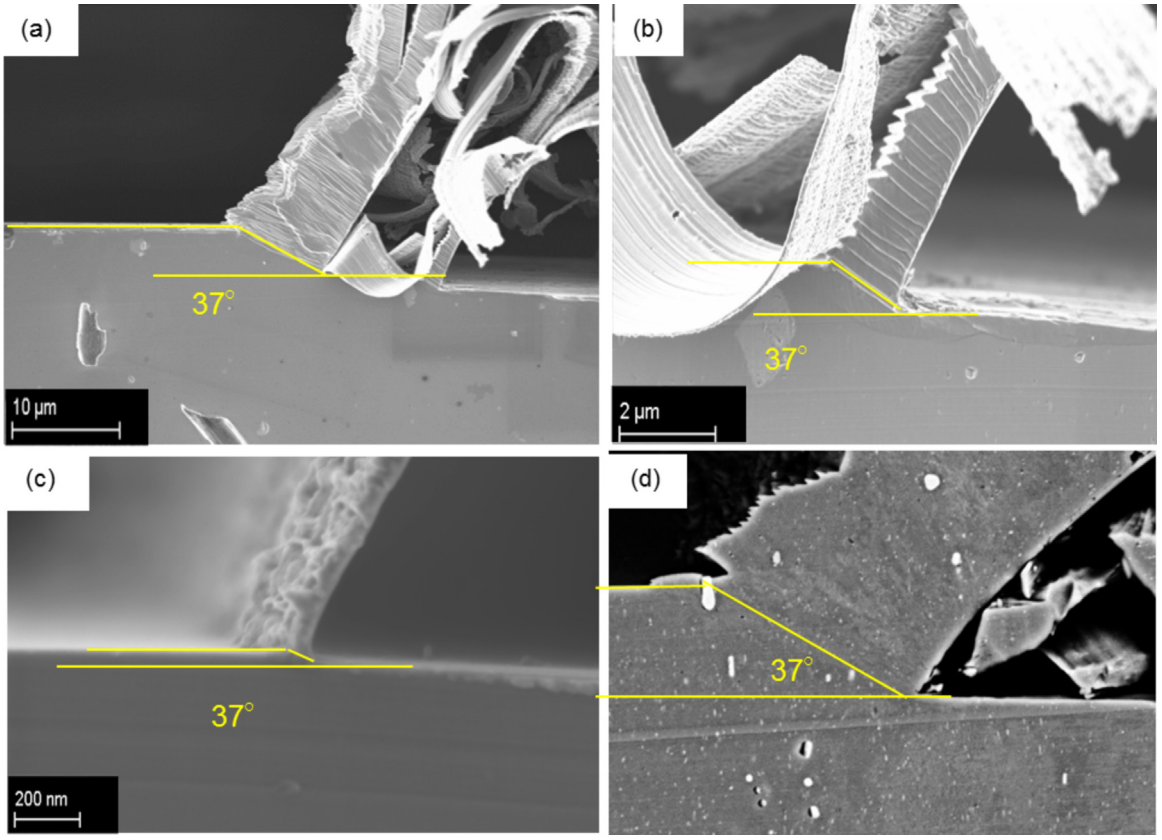

Fig. 7. Cross section secondary electron SEM micrographs displaying the shear angle in the AA2024 aluminium alloy for different slice thicknesses: (a) 5 μm; (b) 1 μm; (c) 50 nm; (d) 5 μm cross sectioned block face ultramicrotomed about 10 μm below the observed block face in (a) which evident of taking the same shear angle through the sliced block face.

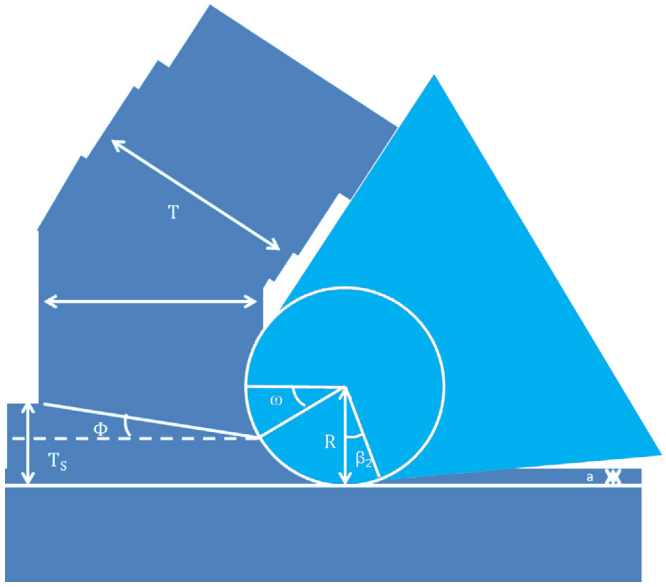

Fig. 8. Schematic diagram showing the force and angle relationships for ultra-thin slicing.

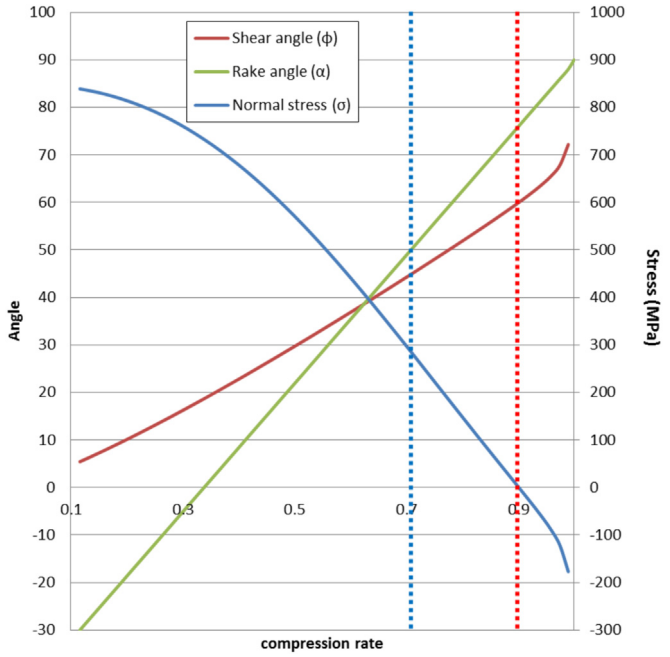

Fig. 9. Relationship between the compression rate, shear angle, Φ, the tool rake angle, α, and normal stress, σ, for cutting the AA2024 aluminium alloy. The vertical dashed lines indicate the conditions when the shear strength and normal stresses become equal (blue line) and the normal force becomes zero (red line). (For interpretation of the references to colour in this figure legend, the reader is referred to the web version of this article.)

layer, as indicated by the following relationships:

$$a = r(1 - \cos\beta_2) = \frac{r(1-\sin\omega)}{10} \tag{6}$$

where a is the thickness of the recovering layer, ω is the angle between the shear force starting point and the cutting direction on the edge of knife, and β_2 is the angle from the perpendicular to the cutting direction on the knife tip and the recovering layer touching the knife tip. The shear angle can then be determined from the following relationship:

$$\tan\varphi = \frac{Ts - [r(1-\sin\omega)]}{T} \tag{7}$$

For slice thicknesses at least 5 × the knife radius, the knife radius does not influence the shear angles significantly, while for slice thicknesses less than 5 × knife radius, the reduction of the shear angles results in increasing damage to the block face.

6. Optimising the cutting conditions

The most important strategy for optimising the cutting conditions is to reduce the forces applied to the block face since these lead to the deformation. The stress at the block face arises from a combination of the cutting force, F_c, and the normal force, F_t, as indicated in the following expression:

$$\sigma = \frac{(F_c\cos\varphi + F_t\sin\varphi)\sin\varphi}{Tb} \tag{8}$$

This stress is strongly influenced by the rake angle. Fig. 9 shows the relationship between the compression rate, the shear and rake angles, and the applied stress. Reduction of the rake angle results in an increase in the shear angle and a reduction of the stress. When, the rake angle is 50°, the shear and normal stresses become equal, while for a rake angle of 76° the normal stress becomes zero. Consequently, if the knife and clearance angles sum to 14°, the damage on the block face is minimised. Further, when the normal stress exceeds the ultimate tensile strength the chip will form by ripping rather than by slicing. When the rake angle exceeds 50°, the normal stress becomes less than the tensile yield stress of the AA 2024 alloy. Hence, damage to the block face might be reduced. However, it is also dependent on the dislocation density, which is readily influenced by deformation on the block face.

In summary, the damage introduced by slicing can be minimised by reducing the slice thickness and the compression rate. This, in turn, depends on the relationship between the shear angle and the rake angle, which is a key aspect for improving the quality of the block face.

Currently, the minimum rake angle of a commercially available diamond knife is 35° however, it is possible to minimise the normal stress. In order to minimise the stresses, the knife can be oscillated to minimise the apparent knife angle [46]. The apparent knife angle (mean knife angle during the oscillation of the knife), α_2, is given by the following equation:

$$\alpha_2 = \frac{V_s}{V_e}\tan(90 - \alpha) \tag{9}$$

where v_s is the traverse speed of the knife and v_e is the velocity normal to the cutting direction. The apparent angle can be applied in the Merchant cutting model and it determines the ultramicrotomy operating conditions for minimum damage on the block face. Notably, the oscillating knife reduces the apparent angle and, thereby, the associated stresses. Additionally, the transverse movement of the knife also causes the local temperature of the material in contact with the knife edge to increase because of the friction between the knife edge and the material, causing the material to soften. The effect of oscillation on reducing chatter and generally improving the surface finish is evident in Fig. 10.

The channelling contrast in BSE images can highlight the damage introduced by block face sectioning because channeling effects arise from a change in electron penetration depth with crystal orientation. These signals are generated from a few nanometres below the surface, rendering the signal sensitive to the atomic perfection of the surface. It is clear from Fig. 11(a) (top) that

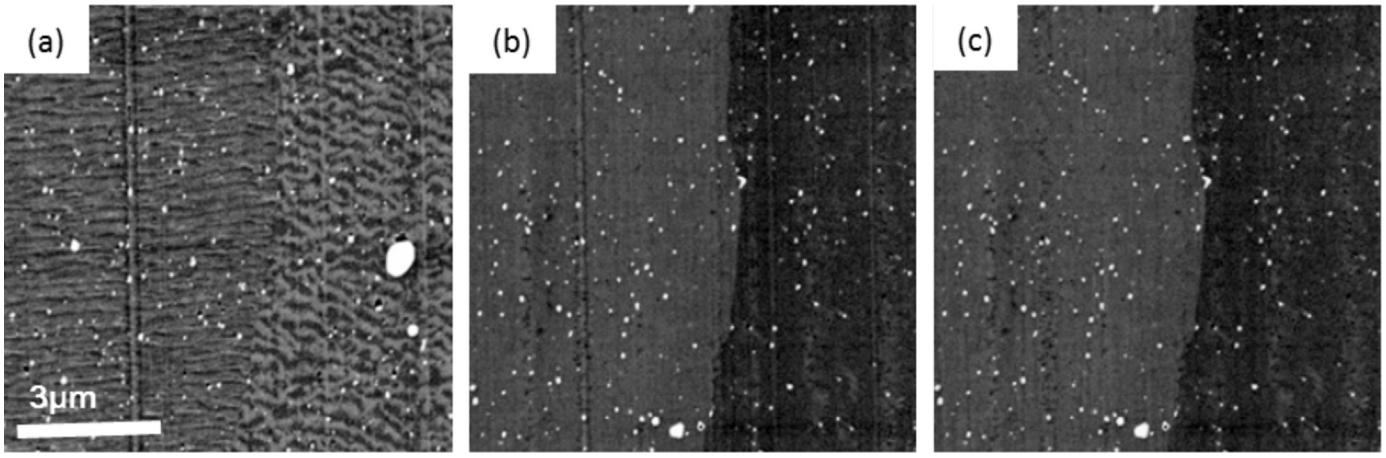

Fig. 10. BSE image of the block face of AA2024 aluminium alloy after slicing with a 35 degree knife and a cutting velocity of 0.04 mms^{-1} using a 15 nm slicing depth: (a) slicing with non-oscillating knife; (b) slicing with oscillating knife; (c) processed image of (b) by applying the artefact-removing method illustrated in Fig. 4.

slicing without oscillating the knife causes a great deal of local disruption that is reflected in a speckle type of BSE contrast. Upon oscillating the knife (Fig.11(a) (bottom)), much more even contrast is obtained that is indicative of a low level of near surface deformation such that the contrast is consistent over many slices enabling artefact free 3D volume reconstructions of the grain contrast to be obtained. Further, the dramatic difference in greyscale level between the first few slices after changing to an oscillating knife (Fig. 11 (b)) suggests that the damage introduced by the non-oscillating diamond knife extends to a depth of around 60 nm (equivalent to four 15 nm thick slices).

Electron backscatter diffraction (EBSD) is often used to determine grain orientations in metallographic sections and is very sensitive to surface deformation. Consequently, as well as being a useful end in itself being able to collect EBSD maps provides a good means of assessing the quality of the block face. Fig. 12 displays EBSD maps of the block face after slicing with and without knife oscillation. A significant rise in the indexing percentage is achieved upon oscillating the knife (from 60 to 92%), demonstrating that good EBSD maps can be collected for aluminium under optimal conditions despite local cutting induced deformation.

7. Applications of ultramicrotomy-based SBFSEM

The previous sections looking at the ultramicrotomy technique have all focused on the AA2024-T3 aluminium alloy, but with care the technique can be applied to a range of material systems. In this section, a number of technologically important systems and applications are examined, and the ease of SBF sectioning is discussed along with practical means of improving the images that can be acquired.

7.1. Intermetallic distribution

SBFSEM provides a cost effective means of mapping the distribution of inclusions and precipitates in 3D over many grains. As an example, Fig. 13 shows 3D images of a cast Al–Si alloy. Iron is a common impurity in aluminium alloys that is not readily removed, and it may have adverse effects on the alloy properties, particularly corrosion property. The solid solubility of iron in aluminium is very low so that most iron forms intermetallics, depending on the presence of other impurities or alloying elements. In this case the AlFeSi intermetallic can have a very significant effect on the mechanical properties of Al–Si alloys. In particular, it decreases ductility because it tends to form as thin platelets which are very

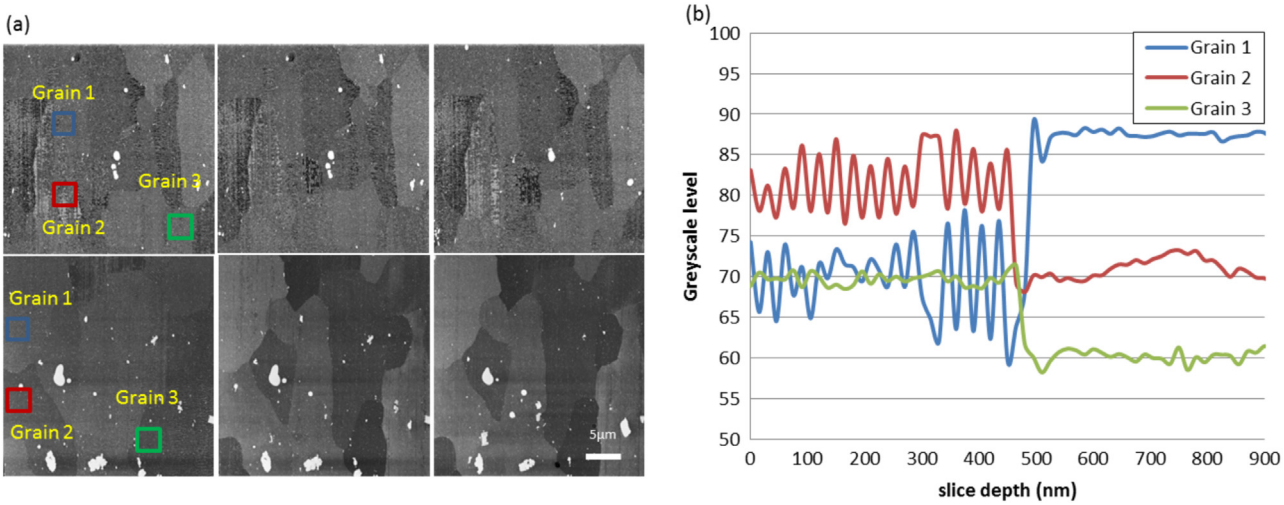

Fig. 11. (a) Series of BSE micrographs of an AA2024 aluminium alloy block face generated using cutting speed of 0.04 mms^{-1} and 15 nm slicing thicknesses. The series of image were generated with a non-oscillating knife (top) and with an oscillating knife (bottom). The images after the 1st, 4th and 30th slicing are shown (left to right) in both cases. (b) Graph showing the variation in greyscale recorded for the three marked grains as a function of slicing depth for the non-oscillating knife (depth < 450 nm) followed by the oscillating knife (depth > 450 nm).

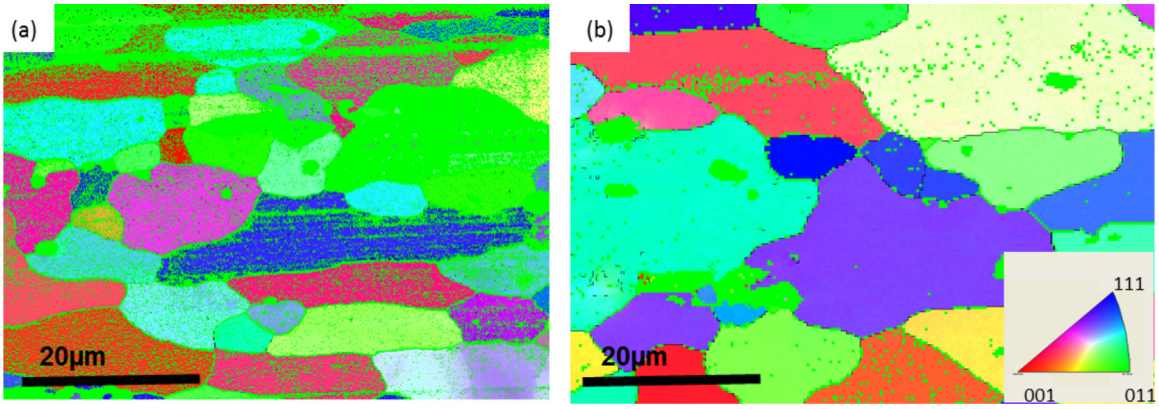

Fig. 12. EBSD maps of the AA2024 aluminium alloy block faces prepared (a) without knife oscillation and (b) with an oscillating knife using a slicing thickness of 15 nm. Non indexable points are shown in green. (For interpretation of the references to colour in this figure legend, the reader is referred to the web version of this article.)

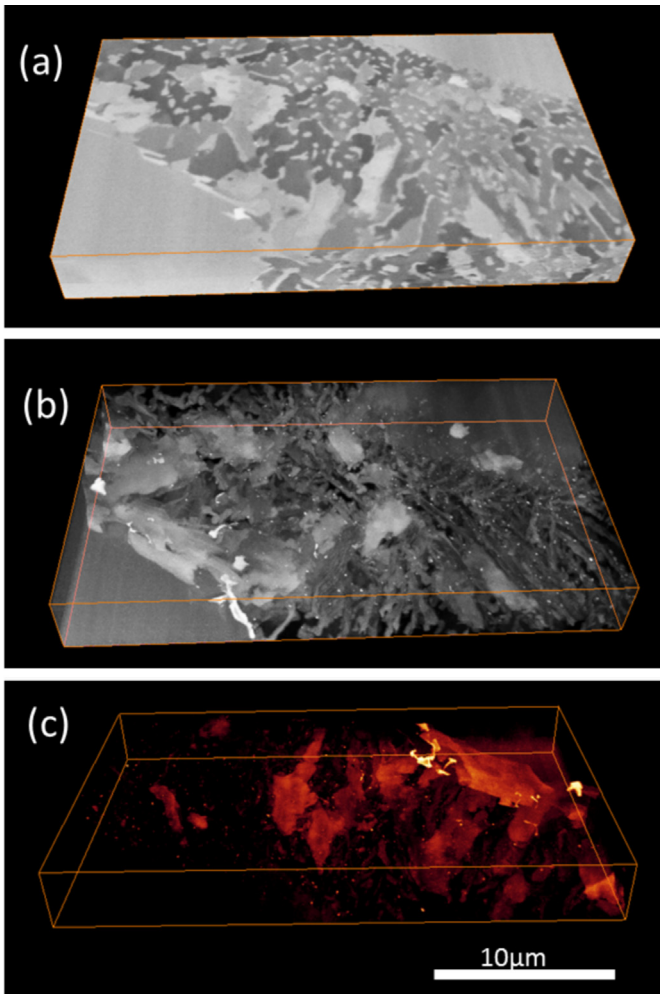

Fig. 13. 3D reconstructed image of the cast AlFeSi alloy acquired using an oscillating knife and cutting speed of 0.04mm s^{-1}: (a) the surface view; (b) semi-transparent 3D view; and (c) thresholded view showing only the Fe enriched particles, the brighter the appearance the higher the iron content.

brittle and bond weakly to the matrix. In addition to influencing the mechanical properties, it also affects the corrosion resistance and surface quality because it is cathodic with respect to the matrix. The 3D images of Fig. 13 provide information on the compositional variation, volume fraction, distribution and preferential direction of the Al_5FeSi intermetallic, which is essential for the microstructural control of the particles.

Interest in magnesium alloys has increased markedly in recent years due to their combination of specific strength, high dimensional stability, good machinability, high castability and their recyclability particularly for applications where low weight and high strength are required. Unfortunately, many magnesium alloys are characterized by poor corrosion resistance. One of the primary reasons for the poor corrosion resistance of magnesium alloys is the internal galvanic corrosion generated by intermetallics or impurities. Consequently, the distribution of the intermetallics is critical in understanding the corrosion behaviour of Mg and its alloys. Generally, steps such as electropolishing, etching and mechanical polishing are use when preparing magnesium specimens for observation in the SEM. These involve contact with aqueous media which can lead to a hydroxide film on the surface which interrupts the SE or BSE signals from the bare surface. Additionally, compared with other metals such as Al or Fe oxide film grows much more rapidly in air. Since serial sectioning is undertaken in the vacuum environment of an SEM, such issues are avoided with SBFSEM. Fig. 14 shows 3D reconstruction of twin roll-cast Mg–Al–Zn alloy, exhibiting the AlMn and AlMg particles. Further, ensuring that ultramicrotomy does not introduce distortion to the block face microstructure by twinning or recrystallisation is of great concern. The EBSD map of AZ31 (Fig. 14(a)), generated with an oscillating knife, was acquired with an indexing rate of 83% and shows no evidence of twinning or recrystallisation. The 3D distribution of AlMg phase (dark gray) at grain boundaries and the flower-shaped AlMn particles are revealed in Fig. 14(b and c). The flower-shaped particle morphologies are attributed to the relatively high cooling rates associated with the twin roll casting process. 3D imaging with EBSD will help determining the growth direction of AlMn particles with respect to the grain orientation of the magnesium matrix and, consequently, advance the understanding of the role of the particles in nucleation during solidification.

Alloy performance and corrosion behaviour are closely related to precipitate size and morphology. Fig. 15 shows the AA2024 aluminium alloy after aging at 180 °C for 20 h, displaying Al_2MgCu needles with an average size of 15 nm width and 200 nm length within the grain, and plate-like precipitates of Al_2MgCu and Al_2Cu with average sizes of 50 nm width and 300 nm length at the grain boundary. Additionally, electron channeling, aligning of precipitates at grain boundaries and the orientation of the needle like precipitates enabled easy distinguishing of the individual grains. The approach enables precise measurement of the volume fractions of the intermetallics in each grain and the morphology of the grain boundary precipitates.

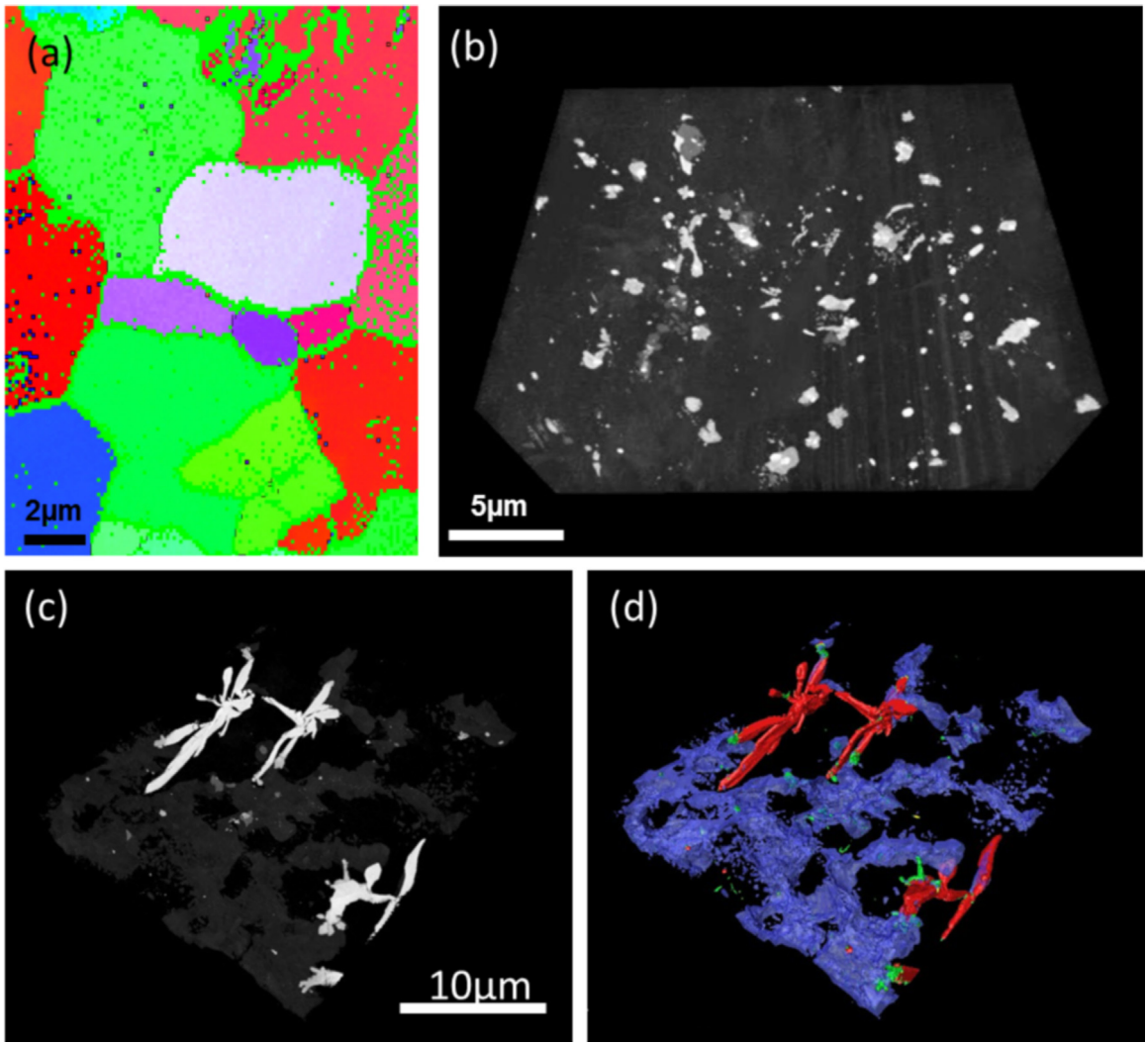

Fig. 14. (a) EBSD map of the AZ31 magnesium alloy prepared with an oscillating knife using a slicing thickness of 15 nm after 200 slices at a cutting speed of 0.04 mm s^{-1}; (b) 3D reconstructed 30 × 30 × 15 μm image of AZ31 magnesium alloy showing the AlMn and AlMg particles; (c) 3D reconstruction of twin roll-cast AZ91 alloy, showing the greyscale level difference between the intermetallic particles; and (d) corresponding segmented 3D reconstruction image of (c), showing the different morphologies of the AlMn(Zn) (red), AlMg (blue) and Si (green) particles. (For interpretation of the references to colour in this figure legend, the reader is referred to the web version of this article.)

7.2. Corrosion

While some aspects of the morphology of corrosion sites can be revealed by 2D SEM, the connectivity from surface to bulk and the 3D interconnected nature of the corrosion requires 3D imaging. Further, the formation of the corrosion product on the surface can mask the underlying structure. SBFSEM is ideal for examining corrosion sites in 3D, especially for light alloys. By way of an example, the immersion testing of the AA2024 aluminium alloy in 3.5 wt% NaCl solution is considered. After 24 h, the intergranular corrosion network extends over tens of microns from the initiation sites with attacked volumes 100 nm or less in width. Thus, capturing the entire corrosion site requires the large field of view and high resolution capability specific to SBFSEM as illustrated in Fig. 16, which shows the propagation of the corrosion front along the grain boundaries. From this it is also clear that the corrosion propagation paths are not affected by the distribution of the Al_2MgCu intermetallics.

7.3. Coatings

Coatings are used for many applications in order to improve the mechanical, thermal or environmental performance of materials. Fig. 17 shows the 3D structure of a porous anodic oxide film on an Al/W alternating multilayer substrate. The specimen was prepared by anodising in phosphoric acid. The distribution of the tungsten layer within the resultant anodic film is compatible with porosity arising mainly from flow of anodic oxide beneath the pore bases towards the cell walls. Thus, the three dimensional image of W helps to understand the oxide flow mechanism during anodic film formation [47].

Fig. 18 shows a 3D reconstruction image of primer paint on a porous anodic oxide film on the AA2024 alloy. The aluminium substrate clearly shows significant electron channelling effect, and the direction of the porous film growth is revealed. Interestingly, morphological variation in the anodic film is revealed in Fig. 19(c). It is evident that the differences in pore size and growth direction are associated with the intermetallic in the alloy.

Zinc magnesium aluminium alloy coatings have been investigated for use on steel because of their potential to provide better corrosion protection than traditional galvanised zinc coatings used in the automobile and construction industries. Studies of the microstructure, mechanical properties and corrosion behaviour of the coating are being undertaken. However, the element

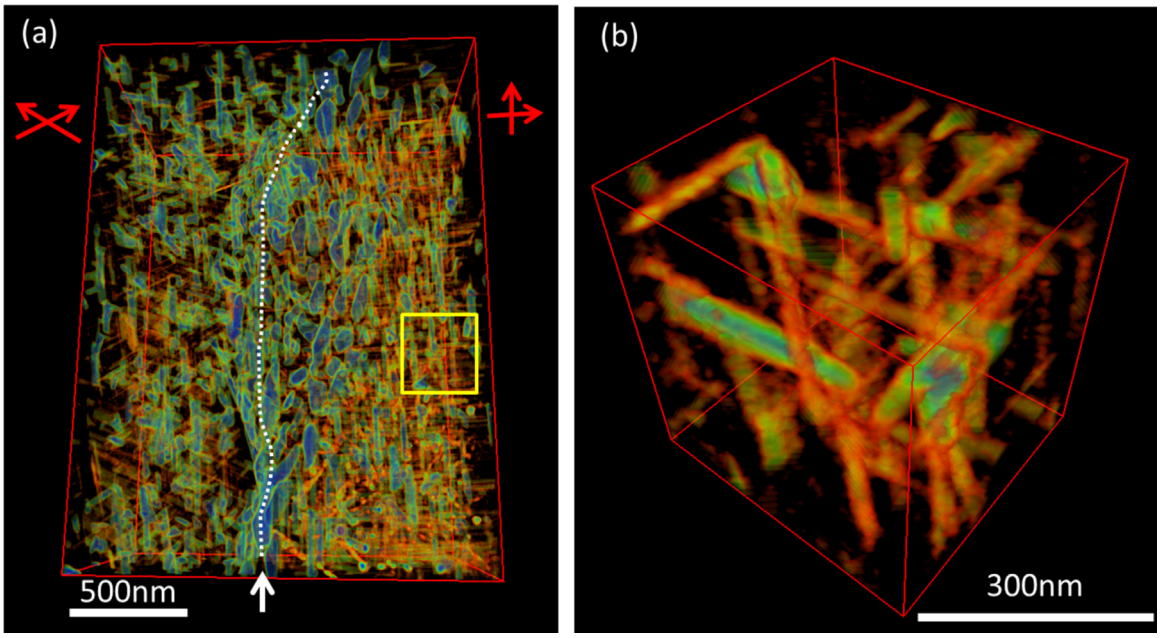

Fig. 15. 3D reconstructions of S phase precipitates in AA2024 alloy (aged for 180 °C for 20 h) compiling 5 nm slices: (a) precipitate distribution across a grain boundary (white dashed line),the red arrows indicate the direction of needle-like precipitates; (b) extracted volume clearly showing the morphology of the needles aligned with the Al {001} planes. (For interpretation of the references to colour in this figure legend, the reader is referred to the web version of this article.)

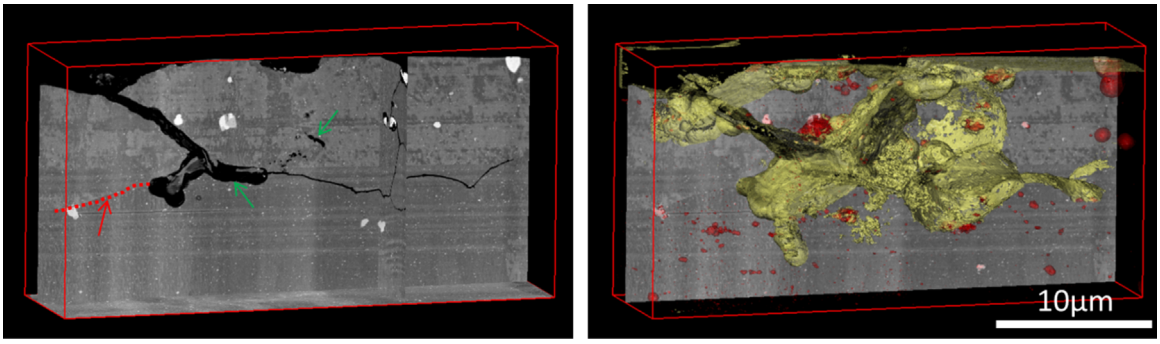

Fig. 16. 3D image of AA2024-T3 alloy after immersion in NaCl solution for 24 h: (a) an orthoslice showing an uncorroded grain boundary (red) alongside extensive corrosion sites (green arrows); (b) the corresponding segmented 3D image revealing the entire corrosion path (yellow) while the intermetallics are labelled red. (For interpretation of the references to colour in this figure legend, the reader is referred to the web version of this article.)

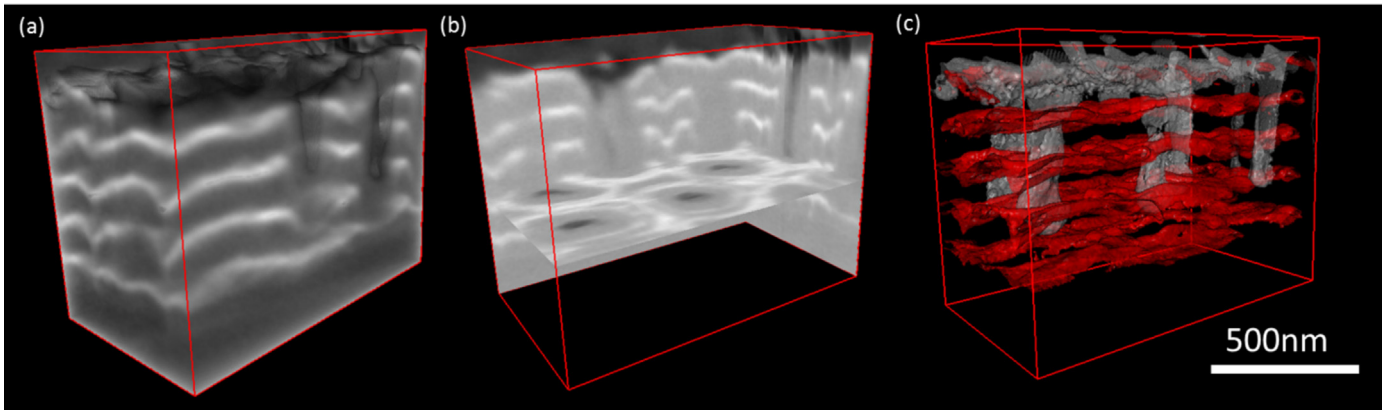

Fig. 17. 3D image of porous alumina anodic film with the multi-layers of tungsten tracers of 15 nm thickness: (a) surface view; (b) orthoslice and (c) segmented 3D reconstruction with tungsten tracers in red and pores in white. (For interpretation of the references to colour in this figure legend, the reader is referred to the web version of this article.)

distributions and the morphology of the coating have a major impact on the anti-corrosion properties. Further, the presence of a eutectic microstructure and the non-uniform distribution of the phases in such a complex microstructure are difficult to investigate with 2D imaging. 3D imaging of the coating helps better understanding of the relationship between the corrosion path and microstructure. Fig. 19 shows the three dimensional reconstructed galvanised steel image.

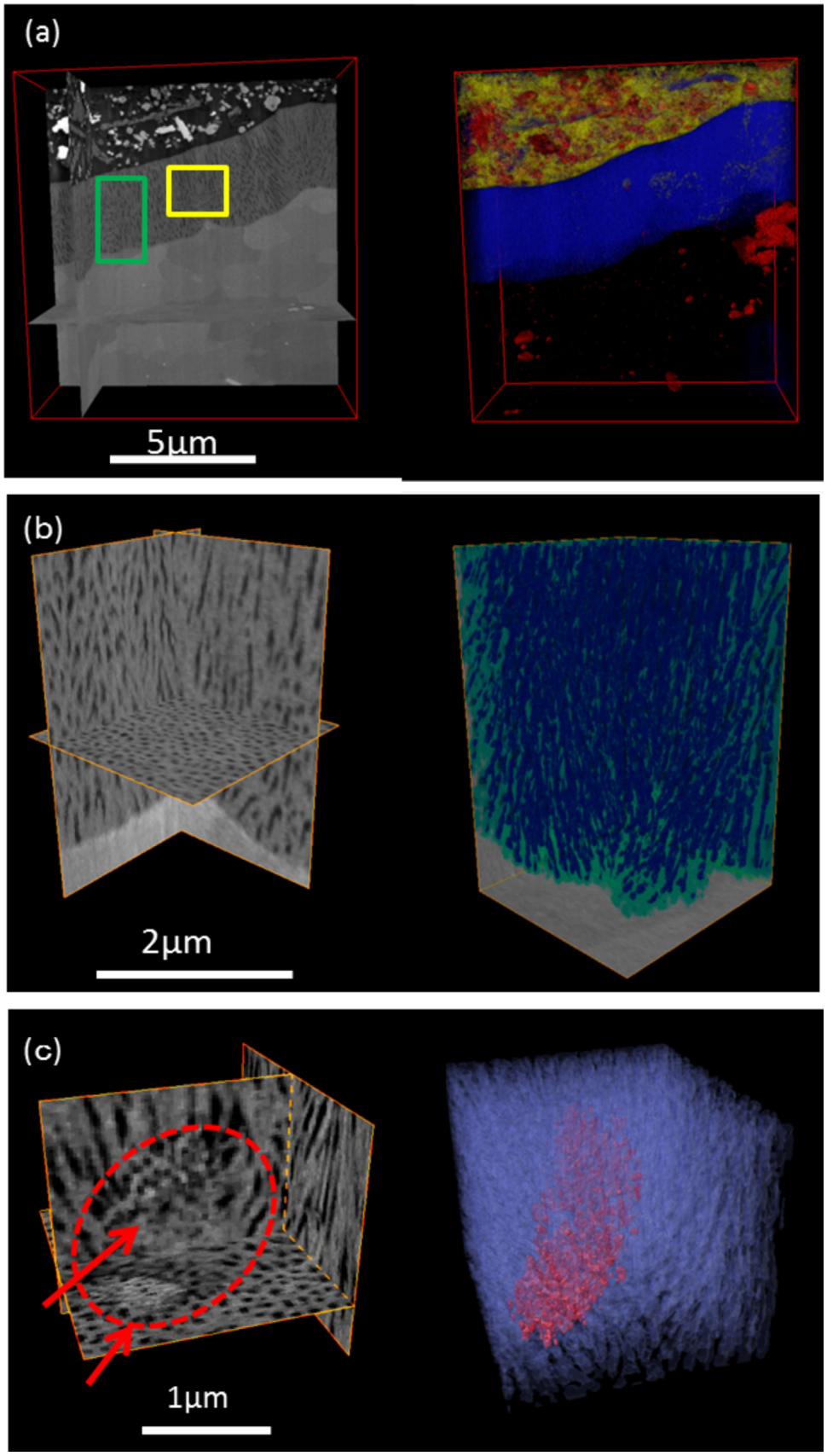

Fig. 18. 3D images of anodised AA2024 alloy and primer paint as orthoslices (left) and segmented views (right): (a) image showing the porous anodic film (blue), the resin (yellow), the intermetallics and paint pigments (red); (b) region in green box showing defect-free anodic film; (c) region in yellow box showing a defect in the film influenced by the initial location of intermetalic (For interpretation of the references to colour in this figure legend, the reader is referred to the web version of this article.).

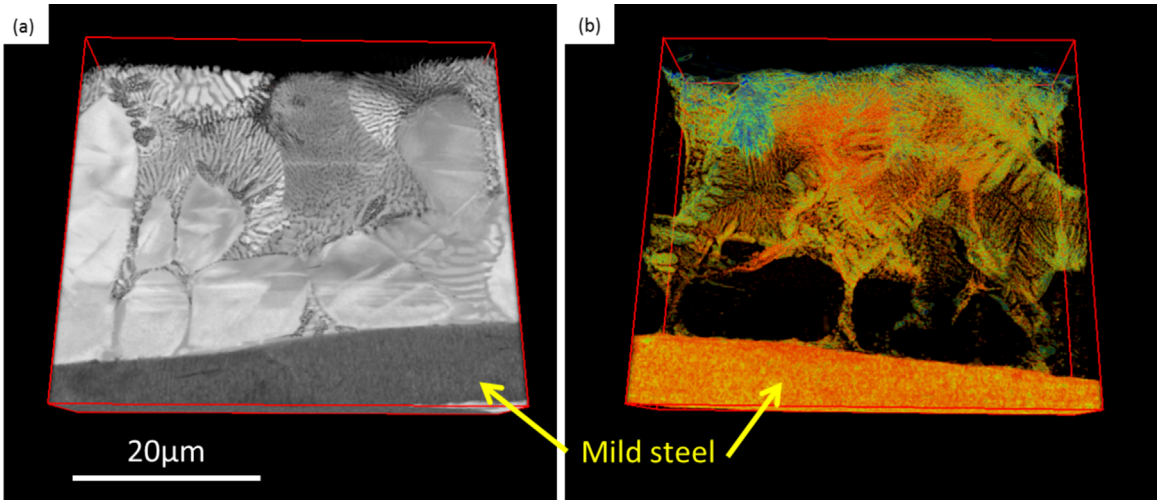

Fig. 19. 3D image of galvanised coating on mild steel: (a) surface view; (b) highlighted Al and Mg enriched eutectic structure attached to the steel substrate.

7.4. Higher hardness materials

Steels present a challenge for serial block face sectioning largely because of their high strength. This increases the cutting force and accelerates wear of the knife that, in turn, changes the knife edge condition in an unpredictable manner. Consequently, it is necessary to increase the slice thickness. Generally, orthogonal slicing is not an efficient method from the energy point of view, with 98% of the total energy during cutting being dissipated as heat [48] that is released into the material and the diamond knife. As mentioned earlier, increasing the temperature of the block lowers the cutting stresses; however, this also increases the dislocation activity near the surface of the block face, causing more smearing. Further, iron has a high chemical affinity with carbon, which leads to reaction of the diamond with the steel and thus increasing wear of the diamond knife.

The lifetime of the knife is dependent on the cutting speed, material and thickness of the slice [49]. Most of the physical and chemical processes involved in the failure mechanisms of the knife are thermally activated. Thus, the cutting temperature is an indirect parameter, depending on direct parameters which fundamentally play an important role on the contact stresses and the relative speed at the tool to block face and tool to chip interfaces. With increasing knife radius, the minimum slice thickness increases and the shear angle reduces. Consequently, the temperature of the knife and block face increase with increasing cutting force. Cooling of the specimen might reduce wear of the diamond knife by reducing the chemical reaction. Also, it assists in minimising the movement of dislocations and, hence, reduces damage to the block face. In order to reduce the temperature of the knife edge, reducing the block face size is effective; however, the magnetic properties of thin sliced steels lead to their preferential passage over the pole piece or lens instead of the vacuum pump system. This can bring about sudden changes of forces or stigmation and, hence, influences the quality of the images. The issue of discarded chip material is a common problem for all specimens; however, the magnetic nature of steel chips directly influences the electron optics more than a non-magnetic specimen.

Given the extensive applications of steel across many industrial sectors, success in minimising damage to the block faces and, hence, successful three dimensional imaging of steel specimens using the SBFSEM will be of interest to many researchers. To achieve this further development of the system is necessary, including reduction of knife angle and chip correcting system, and the introduction of a cryo-system.

8. Conclusions

Serial block face scanning electron microscopy by ultramicrotomy is capable of generating 3D images of engineering materials from light alloys through to metal composites and coatings at nanoscale resolution over large volumes. The optimum combination of knife angle, oscillation and cutting speed is essential for minimising the introduction of damage onto the block face and, consequently, avoiding artefacts in the images. In this paper, alongside the best cutting setting-up, analytical methods for minimising artefacts in the final 3D images have also been explored.

It should be noted that as illustrated here SBFSEM can be combined with EBSD to produce 3D maps of crystalline texture. In addition it can also be combined with EDX to produce nanoscale 3D chemical maps [50]. This paper has demonstrated that SBFSEM should be considered as a useful tool for a wide range of engineering materials science problems and that future developments and the practical input from a wider range of practitioners will extend further the range of samples that can be imaged in this way in 3D.

Acknowledgements

The authors thank EPSRC for support of the LATEST2 Programme Grant (EP/H020047/1) and its associated facilities.

References

[1] D.C. Pease, R.F. Baker, Sectioning techniques for electron microscopy using a conventional microtome, Proc. Soc. Exp. Biol. Med. 67 (1948) 470–474.
[2] A.F. Marshall, D.C. Dobbertin, Cross-sectioning of layered thin films by ultramicrotomy, Ultramicroscopy 19 (1986) 69–73.
[3] R.S. Timsit, J.L. Hutchison, M.C. Thornton, Preparation of metal specimens for HREM by ultramicrotomy, Ultramicroscopy 15 (1984) 371–374.
[4] F. Zörgiebel, H.P. Zeindl, G. Haase, New experiences with ultramicrotomy in electron microscopic investigation of photochromic glasses, Ultramicroscopy 16 (1985) 115–117.
[5] P.R. Lewis, C. Price, Electron microscopy of sym-SBS block polymers, Polymer 13 (1972) 20–26.
[6] G.E. Thompson, R.C. Furneaux, G.C. Wood, J.A. Richardson, J.S. Goode, Nucleation and growth of porous anodic films on aluminium, Nature 272 (1978) 433–435.
[7] R.C. Furneaux, G.E. Thompson, G.C. Wood, The application of ultramicrotomy to the electronoptical examination of surface films on aluminium, Corros. Sci. 18 (1978) 853–881.
[8] J.C. Jesior, How to Avoid Compression II. The Influence of Sectioning

Conditions, J. Ultrastruct. Mol. Struct. 95 (1986) 210–217.
[9] A. Al-Amoudi, J. Dubochet, H. Gnaegi, W. Luthi, D. Studer, J. Microsc., An oscillating cryo-knife reduces cutting-induced deformation of vitreous ultrathin sections, J. Microsc. 212 (2003) 26–33.
[10] A. Al-Amoudi, D. Studer, J. Dubochet, Cutting artefacts and cutting process in vitreous sections for cryo-electron microscopy, J. Struct. Biol. 150 (2005) 109–121.
[11] K.M. Towe, G.H. Hamilton, K.M. Towe, G.H. Hamilton, Ultramicrotome-induced deformation artifacts in densely calcified material, J. Ultrasruct. Res. 22 (1968) 274–281.
[12] E. Maire, P.J. Withers, Quantitative X-ray Tomography, Int. Mater. Rev. 59 (2014) 1–43.
[13] W. Denk, H. Horstmann, Serial block-face scanning electron microscopy to reconstruct three-dimensional tissue nanostructure, PLoS Biol. 2 (2004) 1900–1909.
[14] T. Hashimoto, X. Zhou, C. Luo, K. Kawano, G.E. Thompson, A.E. Hughes, P. Skeldon, P.J. Withers, T.J. Marrow, A.H. Sherry, Nanotomography for understanding materials degradation, Scripta Mater. 63 (2010) 835–838.
[15] ⟨http://www.gatan.com/products/sem-imaging-spectroscopy/3view-system⟩.
[16] ⟨http://www.fei.com/teneo-for-life-sciences/⟩.
[17] J. Lichtman, M. Helmstaedter, Connectomics at the cutting edge: Challenges and opportunities in high-resolution brain mapping, Science 346 (2014) 651.
[18] T. Starborg, N.S. Kalson, Y. Lu, A. Mironov, T.F. Cootes, D.F. Holmes, K.E. Kadler, Using transmission electron microscopy and 3View to determine, Nat. Protoc. 8 (7) (2013) 1433–1448.
[19] T. Anttonen, A. Kirjavainen, I. Belevich, M. Laos, W.D. Richardson, E. Jokitalo, C. Brakebusch, U. Pirvola, Cdc42-dependent structural development of auditory supporting cells is required for wound healing at adulthood, Sci. Rep. 2 (2012) 978.
[20] A. Zankel, B. Kraus, P. Poelt, M. Schaffer, E. Ingolic, Ultramicrotomy in the ESEM, a versatile method for materials and life sciences, J. Microsc. 233 (1) (2009) 140–148.
[21] H. Reingruber, A. Zankel, C. Mayrhofer, P. Poelt, 3D characterization of asymmetric microfiltration membranes, J. Membr. Sci. 372 (2011) 66–74.
[22] H. Koku, R.S. Maier, K.J. Czymmek, M.R. Schure, A.M. Lenhoff, Modeling of flow in a polymeric chromatographic monolith, J. Chromatogr. A 1218 (2011) 3466–3475.
[23] T. Muellner, A. Zankel, C. Mayrhofer, H. Reingruber, A. Höltzel, Y. Lv, F. Svec, U. Tallarek, Reconstruction and characterization of a polymer-based monolithic stationary phase using serial block-face scanning electron microscopy, Langmuir 28 (2012) 16733–16737.
[24] T. Koch, D. Salaberger, A. Zankel, H. Reingruber, A. Steiger-Thirsfeld, Y. Voronko, S. Seidler, Methods for characterizing the 3-D morphology of polymer composites, Macromol. Symp. 315 (2012) 115–124.
[25] X. Zhou, C. Luo, T. Hashimoto, A.E. Hughes, G.E. Thompson, Study of Localized Corrosion in AA2024-T3 Aluminium Alloy Using Electron Tomography, Corros. Sci. 58 (2012) 299–306.
[26] G.E. Thompson, T. Hashimoto, X.L. Zhong, M. Curioni, X. Zhou, P. Skeldon, P. J. Withers, J.A. Carr, A.G. Monteith, Revealing the three dimensional internal structure of aluminium alloys, Surf. Interface Anal. 45 (2013) 1536–1542.
[27] T. Hashimoto, M. Curioni, X. Zhou, J. Mancuso, P. Skeldon, G.E. Thompson, Investigation of dealloying by ultra-high-resolution nanotomography, Surf. Interface Anal. 45 (2013) 1548–1552.
[28] T.J. Marrow, M. Mostafavi, T. Hashimoto, G.E. Thompson, A quantitative three-dimensional in situ study of a short fatigue crack in a magnesium alloy, Int. J. Fatigue 668 (2014) 183–193.
[29] A. Trueman, S. Knight, J. Colwell, T. Hashimoto, J. Carr, P. Skeldon, G. E. Thompson, 3-D tomography by automated in-situ block face ultramicrotome imaging using an FEG-SEM to study complex corrosion protective paint coatings, Corros. Sci. 75 (2013) 376–385.
[30] A.E. Hughes, A. Trinchi, F.F. Chen, Y.S. Yang, I.S. Cole, S. Sellaiyan, J. Carr, P. D. Lee, G.E. Thompson, T.Q. Xiao, The application of multiscale quasi 4D CT to the study of SrCrO4 distributions and the development of porous networks in epoxy-based primer coatings, Prog. Org. Coat. 77 (2014) 1946–1956.
[31] B. Chen, M.G. Sicairos, G. Xiong, L. Shemilt, A. Diaz, J. Nutter, N. Burdet, S. Huo, J. Mancuso, A. Monteith, F. Vergeer, A. Burgess, I. Robinson, Three-Dimensional Structure Analysis and Percolation Properties of a Barrier Marine Coating, Sci. Rep. 3 (2013) 1177.
[32] B. Chen, T. Hashimoto, F. Vergeer, A. Burgess, G.E. Thompson, I. Robinson, Three-dimensional analysis of the spatial distribution of iron oxide particles in a decorative coating by electron microscopic imaging, Prog. Org. Coat. 77 (2014) 1069–1072.
[33] W. Yang, S. Ji, X. Zhou, I. Stone, G. Scamans, G.E. Thompson, Z. Fan, Heterogeneous nucleation of α-Al grain on primary a-alfemnsi intermetallic investigated using 3D SEM ultramicrotomy and HRTEM, Metall. Mater. Trans. A 45 (2014) 3971–3980.
[34] M. Witkowska, G.E. Thompson, T. Hashimoto, E. Koroleva, Assessment of surface reactivity of aluminium AA1050 alloy, Surf. Interface Anal. 45 (2013) 1585–1589.
[35] L. Dwyer, J. Robson, J. da Fonseca, T. Hashimoto, G.E. Thompson, N. Kamp, Constituent Particles and Dispersoids in an Al-Mn-Fe-Si Alloy Studied in Three-Dimensions by Serial Sectioning, Mater. Sci. Forum 765 (2013) 451–455.
[36] T.L. Burnett, S.A. McDonald, A. Gholinia, R. Geurts, M. Janus, T. Slater, S.J. Haigh, C. Ornek, F. Almuaili, D.L. Engelberg, G.E. Thompson, P.J. Withers, Correlative Tomography, Sci. Rep. 4 (2014) 4711.
[37] P.J. Withers, X-ray Nanotomography, Mater. Today 10 (2007).
[38] A. King, G. Johnson, D. Engelberg, W. Ludwig, J. Marrow, Observations of intergranular stress corrosion cracking in a grain-mapped polycrystal, Science 321 (2008) 382–385.
[39] S.D.M. Jacques, C.K. Egan, M.D. Wilson, M.C. Veale, P. Seller, R.J. Cernik, A laboratory system for element specific hyperspectral X-ray imaging, The Analyst 138 (2013) 755–759.
[40] T.L. Burnett, R. Kelley, B. Winiarski, L. Contreras, A. Gholinia, M.G. Burke, P. J. Withers, Large volume Serial Sectioning Tomography using by Plasma Xe Plasma FIB Dual Beam Microscopy, Ultramicroscopy (2015).
[41] M.P. Echlin, A. Mottura, T.M. Pollock, The Tri-beam system: femtosecond laser based tomography in a dual-beam FIB, Microsc. Microanal. 17 (2011) 958–959.
[42] T. Hashimoto, G.E. Thompson, M. Curioni, X. Zhou, P. Skeldon, Three dimensional imaging of light metals using serial block face scanning electron microscopy (SBFSEM), Mater. Sci. Forum 765 (2013) 501–505.
[43] M.E. Merchant, Mechanics of the metal cutting process. I, J. Appl. Phys. 16 (1945) 267–275.
[44] M.E. Merchant, Mechanics of the metal cutting process. II, J. Appl. Phys 16 (1945) 318–324.
[45] T.R. Matzelle, H. Gnaegi, A. Ricker, R. Reichelt, Characterization of the cutting edge of glass and diamond knives for ultramicrotomy by scanning force microscopy using cantilevers with a defined tip geometry, J. Microsc. 209 (2003) 113–117.
[46] D. Studer, H. Gnaegi, Minimal compression of ultrathin sections with use of an oscillating diamond knife, J. Microsc. 197 (2000) 94–100.
[47] S.J. Garcia-Vergara, P. Skeldon, G.E. Thompson, H. Habazaki, A flow model of porous anodic film growth on aluminium, Electrochim. Acta 52 (2006) 681–687.
[48] G. Barrow, A review of experimental and theoretical techniques for assessing cutting temperatures, CIRP Ann. 22 (1973) 203–211.
[49] J.A. Arsecularatnea, L.C. Zhanga, C. Montross, Wear and tool life of tungsten carbide, PCBN and PCD cutting tools, Int. J. Mach. Tools Manuf. 46 (2006) 482–491.
[50] A. Zankel, H. Reingruber, H. Schroettner, 3D elemental map in ESEM, Imaging Microsc. 2 (2011) 35–37.